Correlation-based Shack-Hartmann wavefront sensing with extended source beacon

Takao Endo, Yoshichika Miwa, Toshiyuki Ando

Information Technology R&D Center, Mitsubishi Electric Corporation
5-1-1 Ofuna, Kamakura, Kanagawa 247-8501, Japan

Yasutaka Fujii

Kamakura works, Mitsubishi Electric Corporation
325 Kamimachiya, Kamakura, Kanagawa 247-8520, Japan

Takashi Takanezawa and Yutaka Ezaki

Communication Systems Center, Mitsubishi Electric Corporation
8-1-1 Tsukaguchi-Honmach, Amagasaki, Hyogo 661-8661, Japan

ABSTRACT

Adaptive and active optics were originally developed in the field of astronomy to remove the image aberration induced by wavefronts propagating through Earth's atmosphere, and by gravitational deformation or misalignment of the telescope optics. A conventional wavefront sensor (WFS) generally requires a single or multiple point source beacons, either a natural guide star or laser guide star, as the reference wavefront. However, for passive, remote imaging applications, such a reference source is not generally available. Therefore, we have already developed extended-scene Shack Hartmann (SH) WFS for space-based and ground-based active/adaptive optics systems. In this paper, we discuss the correlation-based wavefront detection algorithm and the preliminary results of the prototype SH-WFS. In order to compensate up to the fifth order of Zernike polynomial with an accuracy of $5/100\ \lambda$, we set the number of pupil divisions to 12×12 and the number of pixels per sub-aperture to 100×100 pixels for prototype SH-WFS. In this design, the accuracy of $1/50$ pixel is required to measure the sub-pixel displacement of the sub-image, and then we evaluated the accuracy of the sub-pixel shift for prototype SH-WFS in the laboratory. As a result, we confirmed the accuracy of $1/69$ pixels can be satisfied. This corresponds to an accuracy of less than $4/100\ \lambda$ of the Zernike polynomial.

1. INTRODUCTION

Adaptive and active optics were originally developed in the field of astronomy to correct wavefront errors ceased by atmospheric turbulence and gravitational deformation or misalignment of optical elements. In order to measure the incoming wavefront incident on the optical system, Shack-Hartmann (SH) Wavefront Sensor (WFS) is generally required a single or multiple reference point source beacons in both adaptive and active optics systems. In the field of astronomy, the natural guide star (NGS) or artificial laser guide star (LGS) have been used as the reference wavefront. However, for passive, remote imaging applications, such a reference source is not generally available. For this reason, wavefront sensing techniques with referred a diffuse, spatially extended light source as a reference wavefront has been reported in the last decade [1, 2, 3, 4].

In particular, we are also developing the correlation-based wavefront sensor for space-based remote imaging telescope such as Earth observation satellite. In this sensor, the extended light source as the reference wavefront is observed image itself. Hence, the reference wavefront is no longer restricted to a point light source, so that the field of wavefront sensing will be utilized in various application.

For example, in the case of tracking resident space objects (RSOs) or the Sun with a ground-based optical telescope as shown in Fig. 1, the moving object itself can be utilized to probe the atmosphere above the telescope. The wavefront aberration obtained with the correlation-based WFS should be corrected by a deformable mirror (DM) in a conventional adaptive optics system. In the case of tracking RSOs, the reference wavefront should be measured at the speeds over 1 kHz frame rates because the non-sidereal tracking required to follow orbiting objects results in high slew
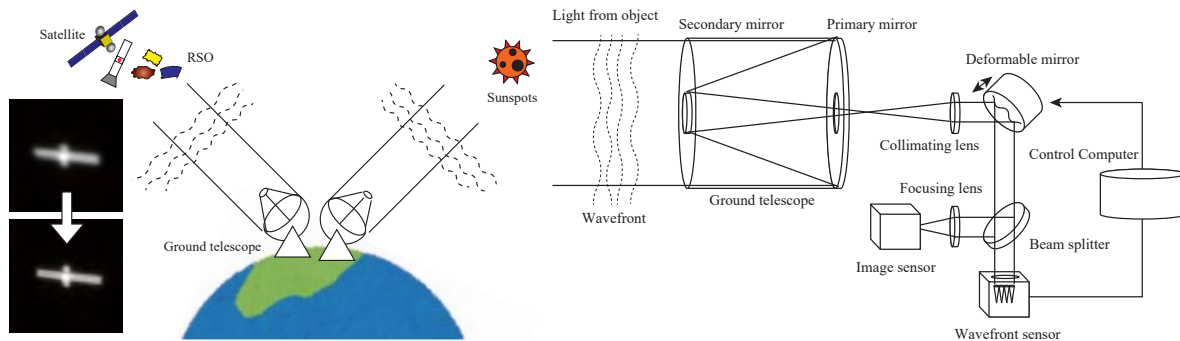
Fig. 1: Example of wavefront sensing with extended light source – adaptive optics

speeds. On the other hand, it should be noted that wavefront sensing using the correlation of multiple sunspots on the Sun surface has already been utilized in the field of sidereal tracking applications [2].

Furthermore, in the field of remote imaging of earth observation, the correlation-based WFS is quite useful because a reference point source is not generally available on the earth's ground [1, 3]. By using observed ground image itself as a reference wavefront, the obtained wavefront indicates the wavefront aberration due to thermal deformation and the misalignment of optical systems in a space-based telescope. Reflective optics for space telescopes generally consist of two hyperbolic mirrors, such as a primary mirror and a secondary mirror. In order to correct the wavefront errors caused by the misalignment of these mirrors, the normal of the secondary mirror is aligned to the normal of the optical axis of the telescope. As a result, the focal and coma aberrations can be subtracted from the total amount of wavefront errors.
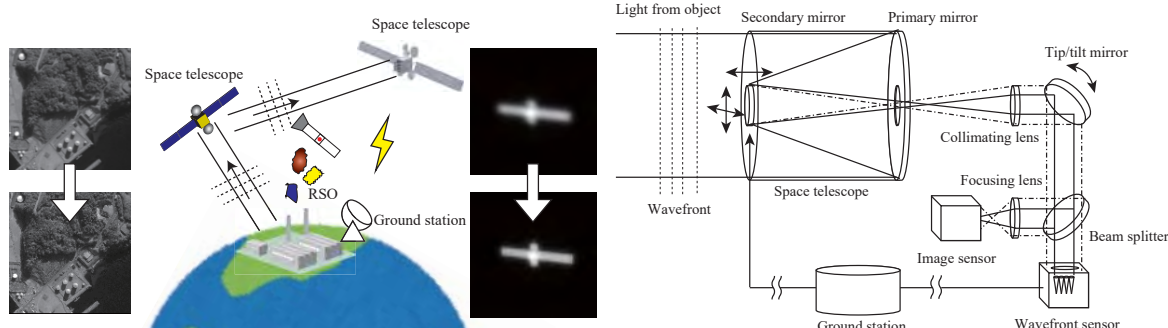

Fig. 2: Example of wavefront sensing with extended light source – active optics

In the field of space-based space situational awareness (SSA), image restoration or deconvolution from wavefront sensing is also useful for high-resolution imaging. In the same way as described above, the static aberration in the fixed optics is also calculated from the wavefront of the entrance pupil. Therefore, it is possible to obtain the detailed feature of the true object by removing the degraded point spread function (PSF) from the observed image.

The wavefront sensing algorithm of SH-WFS, which refers to an expanded light source instead of a point source, is generally called imaging SH-WFS or extended scene SH-WFS. In this paper, we discuss the correlation-based wavefront sensing algorithm and the preliminary results of the prototype SH-WFS for onboard satellite.

2. PRINCIPLE OF WAVEFRONT SENSING

2.1 Shack-Hartmann wavefront sensor

Interferometers are one of the most common instruments used to characterize the wavefront aberrations of optical systems. Because the measurement principle of the interferometer depends on the optical path length, the accuracy of wavefront sensing is affected by the disturbance of the ambient environment. On the other hands, SH-WFS is fundamentally based on the geometrical optics, and consists of an array of lenses for wavefront division and typically CCD or CMOS image sensor used for spot position (local wavefront tilt) measurement.

(a) Point light source

(c) Extended light source

Incoming beacon

Shack-Hartman Wavefront Sensor

(b) Point source image
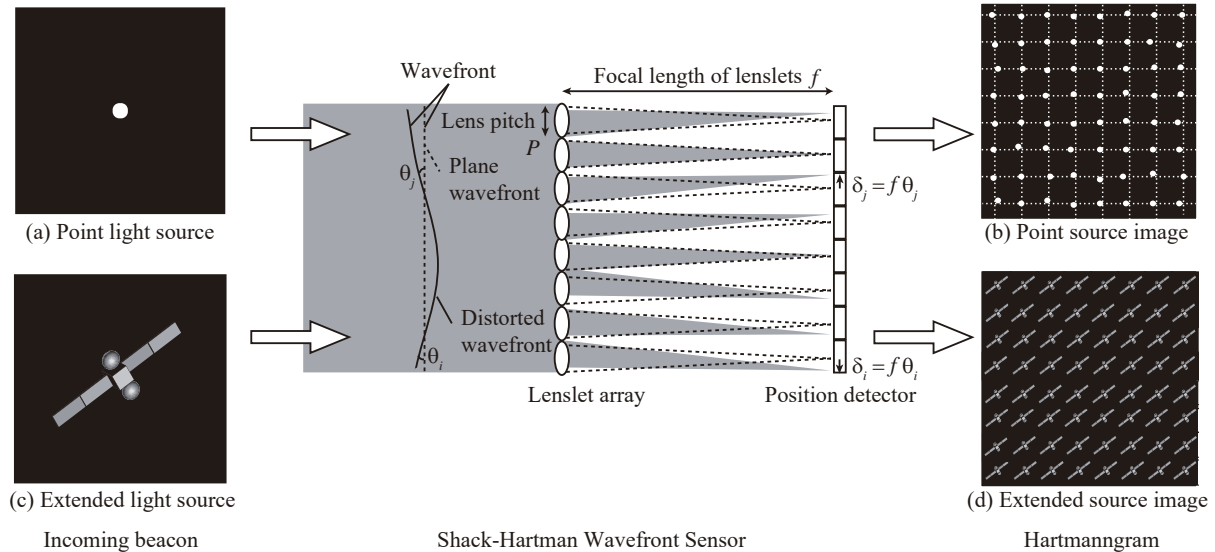
(d) Extended source image

Hartmanngram

Fig. 3: Wavefront measurement principle of SH-WFS.

At first, we explain the principle of measuring the wavefront of SH-WFS as shown in Fig 3. The SH-WFS is a pupil plane measurement of local wavefront slopes (the first derivative of the wavefront) within a sub-aperture defined typically by a lenslet array. A conventional SH-WFS generally requires a single or multiple point source beacons, either a NGS or an artificial LGS, as the reference wavefront. The segmented incident wavefront focuses a spot onto an array of detectors in the lenslet focal plane. The positions of the focal spots (generally called Hartmann spots or Hartmanngram) on the position detector are proportional to local wavefront slope.
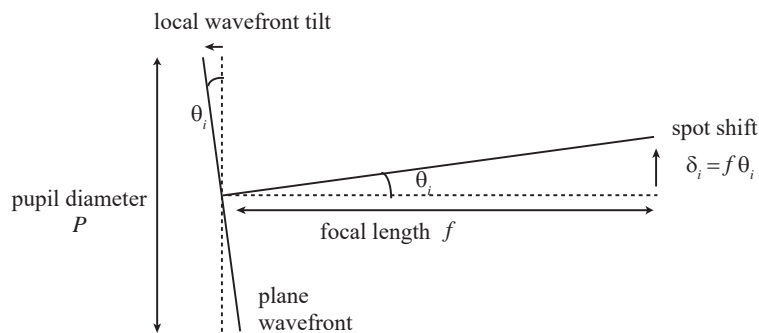

Fig. 4: Relation between focal spot and local wavefront tilt

Fig. 4 shows the relation between the position of the spot focused on the detector and the local wavefront tilt of

sub-aperture. The spot position δ_i is related to the local wavefront tilt θ_i over the i th sub-aperture as follow

$$\delta_i = f\theta_i \tag{1}$$

where f is the focal length of the sub-aperture lens. Since the brightness distribution of the focal spot shows symmetrical for a point source beacon, the spot position δ is calculated by the centroid of the spot brightness on the detector plane [5].

$$\bar{x}_i = \frac{\sum x I_i(x)}{\sum I_i(x)} \tag{2}$$

$$\delta_i = \bar{x}_i - \bar{x}_{\text{Ref}} \tag{3}$$

Although, SH-WFS has been utilized for both drive control of the ground telescope and the ground-based calibration of the space telescope so far [6, 7, 8, 9], it should be noted that the reference wavefront of WFS for these applications requires a point light source such as NGS or laser light source. In wavefront sensing with referred to a point light source, the accuracy of position evaluation was satisfied less than $5/100 (= 1/20)$ pixel.

2.2 Extended-scene SH-WFS

Next, we also explain the principle of measuring the wavefront of extended scene SH-WFS as shown in Fig 3. By using the extended object as a beacon light source, a set of extended sub-images rather than symmetric spots is generated on the focal plane. Since extended sub-images are asymmetric, the spot positions cannot be estimated by calculating the centroids of these sub-images using equation (2)-(3).

For this reason, the accuracy of the wavefront sensing with an extended source depends on an algorithm to estimate the relative position of extended sub-images. In order to obtain the alignment between a pair of images, one approach is to shift the images relative to each other and to look at how much the pixels agree. The simplest alignment between two images is to shift one image relative to the other. In order to use pixel-to-pixel matching, often called the direct method, an appropriate error metric first should be selected to compare the images.

A least-squares solution to this problem is to find the minimum of the sum of squared differences (SSD) function as follows

$$E_{\text{SSD}}(\delta_i) = \sum [I_i(x+\delta) - I_{\text{Ref}}(x)]^2 = \sum \epsilon^2 \tag{4}$$

where I_{Ref} is template sub-image at pixel locations x, I_i is i th sub-image, δ is the displacement and ϵ is called the residual error or the displaced frame difference.

On the other hands, an alternative to minimize the error metric is to perform correlation to maximize the cross correlation of the two aligned images,

$$E_{\text{CC}}(\delta_i) = \sum I_{\text{Ref}}(x) I_i(x+\delta) \tag{5}$$

The cross correlation function is also obtained by Fourier convolution theorem. Fourier-based convolution is often used to accelerate the computation of image correlations.

The Fourier spectrums of i th sub-image I_i and template sub-image I_{Ref} are calculated as

$$\mathcal{I}_i(u) = \mathcal{F}[I_i(x)] \tag{6}$$

$$\mathcal{I}_{\text{Ref}}(u) = \mathcal{F}[I_{\text{Ref}}(x)] \tag{7}$$

where $\mathcal{F}$ denotes notation of Fourier transform. The cross-correlation spectrum $\mathcal{P}$ in the Fourier domain is defined as

$$\mathcal{P}(u) = \mathcal{I}_{\text{Ref}}(u) \mathcal{I}_i^*(u) \tag{8}$$

Therefore, the Fourier transform of the cross-correlation function E_{CC} can be written as

$$\begin{aligned}
\mathcal{F}[E_{\text{CC}}(\delta_i)] &= \mathcal{F}\left[\sum I_{\text{Ref}}(x) I_i(x+\delta)\right] \\
&= \mathcal{I}_{\text{Ref}}(u) \mathcal{I}_i^*(u) \\
&= \mathcal{P}(u)
\end{aligned} \tag{9}$$

because the convolution is defined as the summation of one signal with the reverse of the other.

3. PROTOTYPE DESIGN OF EXTENDED SCENE SH-WFS

3.1 WFS design for space-based telescope

In this section, we first introduce the design concept of prototype correlation-based SH-WFS. Space-based remote imaging or space-based SSA satellites need to correct for static aberration in the fixed optics of the space telescope. Therefore, the purpose of the onboard wavefront sensor is to quantitatively measure the wavefront error during in-flight operation. The wavefront error is represented as the sum of the modes of Zernike polynomial. For example, in order to correct the wavefront errors caused by the misalignment of these mirrors, the normal of the secondary mirror is aligned to the normal of the optical axis of the telescope. As a result, the focal and coma aberrations can be subtracted from the total amount of wavefront errors.

Because of the central obscuration by the shade of secondary mirror, it is difficult to align between the center of telescope pupil and the origin of Zernike mode. In order to reduce the estimation errors of Zernike mode, the prototype SH-WFS was designed to measure up to fifth order of Zernike mode. The dynamic range of prototype WFS is designed as the range of $\pm 2\lambda$ because the wavefront errors due to thermal deformation and the misalignment of optical systems are assumed to be the order of the wavelength. On the other hands, the frame rate was designed as 10 fps or less because the shapes or positions of the mirror are not corrected in real-time operation.

Table 1: Specification of the prototype SH-WFS

Item		Specification
CMOS	Pixel pitch	5.3 [μm/pixel]
	Format	1280×768 [pixels]
	Data bit	10 [bit]
	Quantum efficiency	0.35 [e$^-$/photon]
	Readout noise	6.5 [e$^-$ r.m.s]
MLA	Lens pitch P	440 [μm]
	Number of sub-apertures	12×12
	F-number F_{ML}	11.4
	Spectral radiance B_λ	20 [W/m^2 ster μm]
	Filter band width $\Delta\lambda$	100 [nm]
	Exposure	1–100 [ms]
	Field stop	4.5×4.5 [mm]
	Reference cell	64×64 [pixels]

3.2 Optical layout

In order to evaluate the aberrated PSF of the space-based telescope during in-flight operation, at least three elements of (1) a reference light source, (2) a telescope to be measured, and (3) an onboard WFS are required. Therefore, the elements of (1) and (2) should be also prepared for a ground-based verification. Fig. 5 shows the comparison between the optical elements of in-flight operation and that of ground-based verification. The extended light source for in-flight operation is Earth's surface or RSO illuminated by the Sun. Hence, in ground-based verification, we also designed (1) an extended light source consisting of a light source, an illumination optics, and object slides, and (2) a telescope optics consisting of an aperture stop and imaging lenses.

The optical layout for ground-based verification is shown in Fig. 6. In the figure, the light propagates in the direction from left to right. The optical elements such as the light source, illumination optics, object slides, the telescope optics, and SH-WFS are placed on the optical rail in this order.

Fig. 7 (a)-(c) shows the simulated Hartmanngram obtained by a space telescope with central obscuration. Note that since the onboard WFS requires redundancy for in-flight operation, it is designed to be compatible with both conventional point light sources and extended light sources.
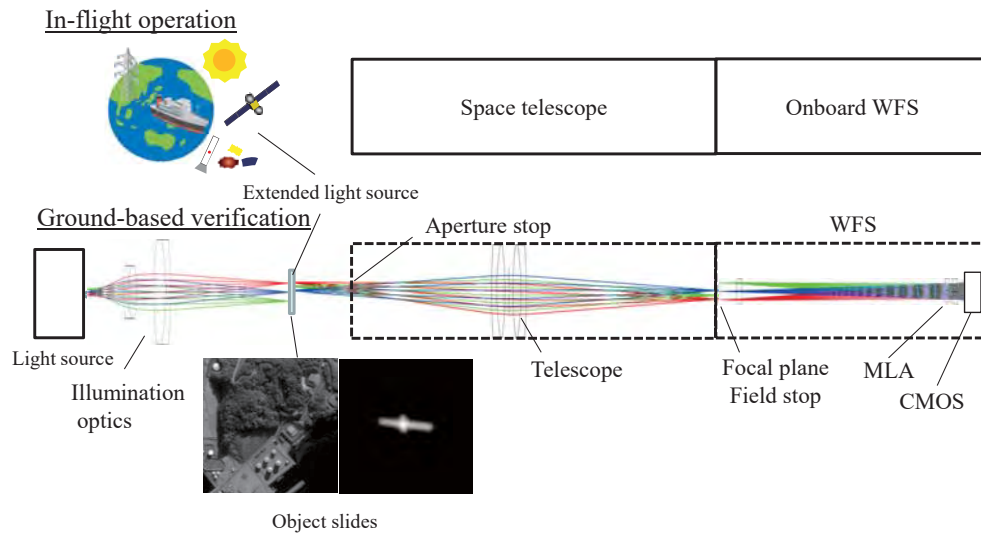
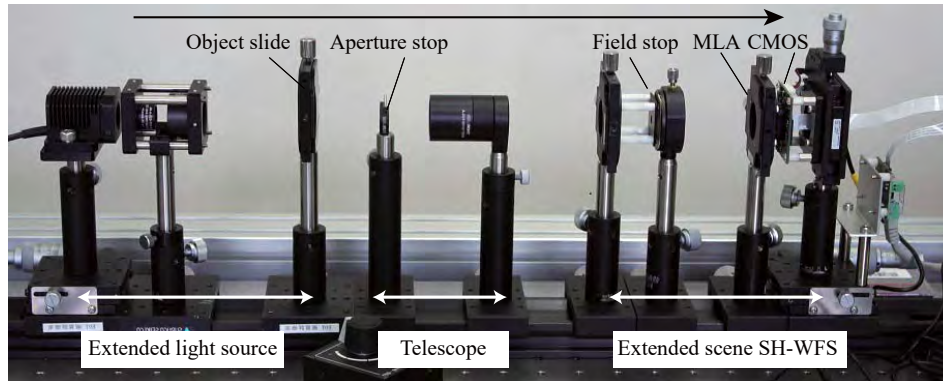Fig. 5: Schematic drawing of optical layout for in-flight / ground-based verification.

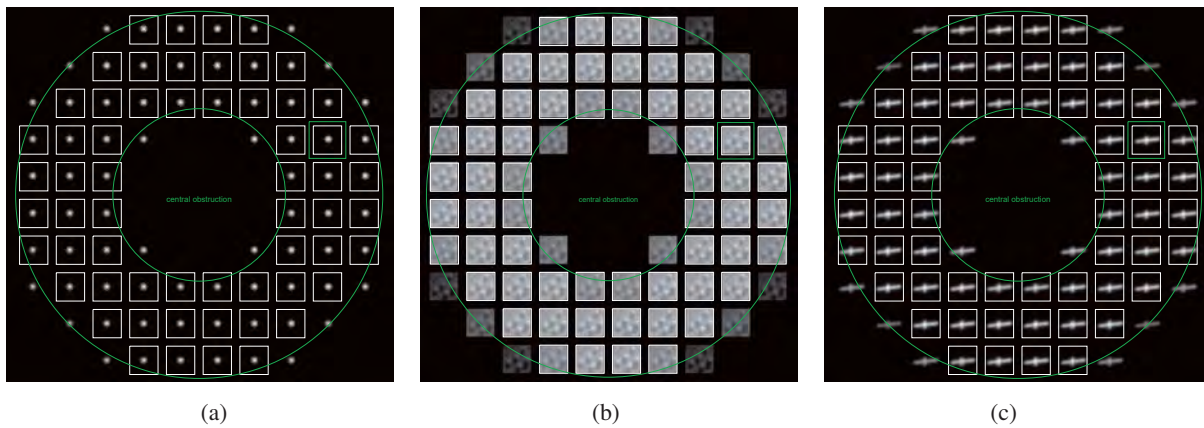Fig. 6: Experimental optics of extended scene SH-WFS.

(a)   (b)   (c)

Fig. 7: Simulated Hartmanngram – (a): Point light source, (b)–(c): Extended light source.

4. EXPERIMENTAL EXAMPLE

4.1 Cross-correlation Hartmanngram

In order to verify the wavefront sensing accuracy of the onboard wavefront sensor, we prepared the experimental optics in a laboratory as shown in Fig. 6. Since the central obscuration mask is not placed at telescope's pupil in the laboratory optics, sub-images of Hartmanngram are also located at the center of the area sensor.

The red rectangle in Fig. 10 shows the actual area of the image sensor, the outer green circle and the inside one shows the entrance pupil and the area of central obscuration for a space telescope, respectively. The specitication of a data bit of area sensor is 10 bit readout, however, an image capture was restricted in the range of up to 8 bit in this measurement. Therefore, we obtained the frame data of Hartmanngram with 8 bit linearity.

Fig. 8 shows the calculation flow to estimate the relative displacement. First, the reference cells as template sub-image must be selected from the part of the same Hartmanngram (Fig. 8b). Next, we perform the Fourier transform of both image I_i and I_{Ref} described in Section 2.2 (Fig. 8c). After conjugating the second one, we thus calculate the cross-correlation spectrum of equation (8) from multiplying both transforms together (Fig. 8d). Finally, the cross-correlation function is obtained from the inverse Fourier transform of the cross-correlation spectrum (Fig. 8e).
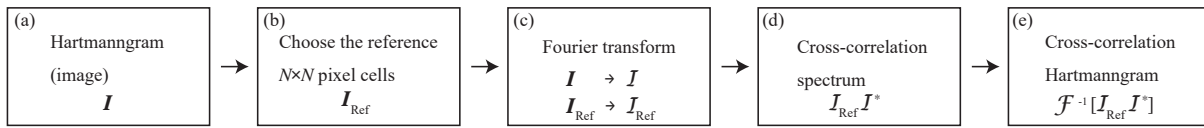

Fig. 8: Calculation flow 1

In the experiment, we used the object slide printed the photograph of the earth's ground as the extended light source. Fig. 9(a) shows the photograph of the seaside in Kanagawa prefecture, Japan, and white box in Fig.9(a) is the area of object slide in this experiment. Because the image of Fig. 9(a) has multiple gas holders that align diagonally, it is easy to assume that multiple sub-peaks also align a diagonal direction in the auto-correlation function. Fig. 9(b) shows the 3D view of the auto-correlation function calculated from Fig. 9(a). Because multiple sub-peaks can be seen in addition to the main peak at the center of Fig. 9(b), we confirm that the obtained correlation function is quantitatively applopriate.

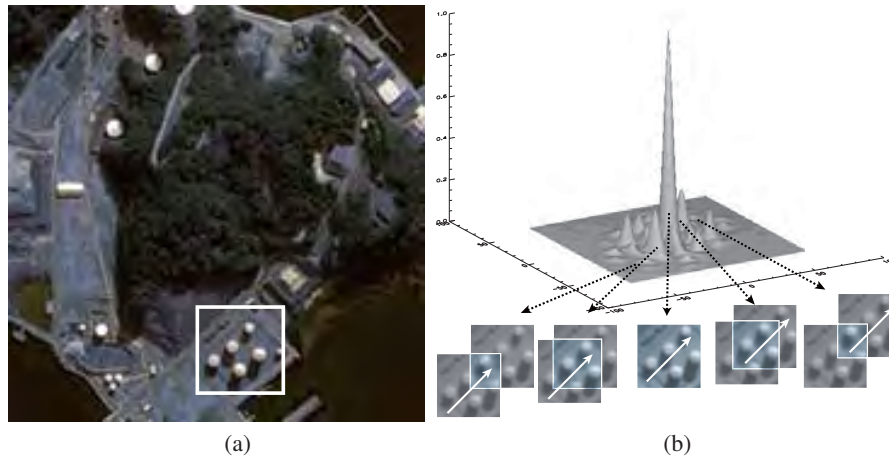(a)   (b)

Fig. 9: Example of object slide and 3D view of auto-correlation function

The reference cells located at $(p,q) = (4,2)$ off-axis position are selected as template sub-image because the center of the entrance pupil is generally obscured by the secondary mirror of the space telescope. Fig. 10 (a) and Fig. 10 (b) show the all sub-images and template sub-image of Hartmanngram, respectively.

Next, the result of the cross-correlation between Fig. 10(a) and Fig. 10(b) and the auto-correlation of Fig. 10(b) are
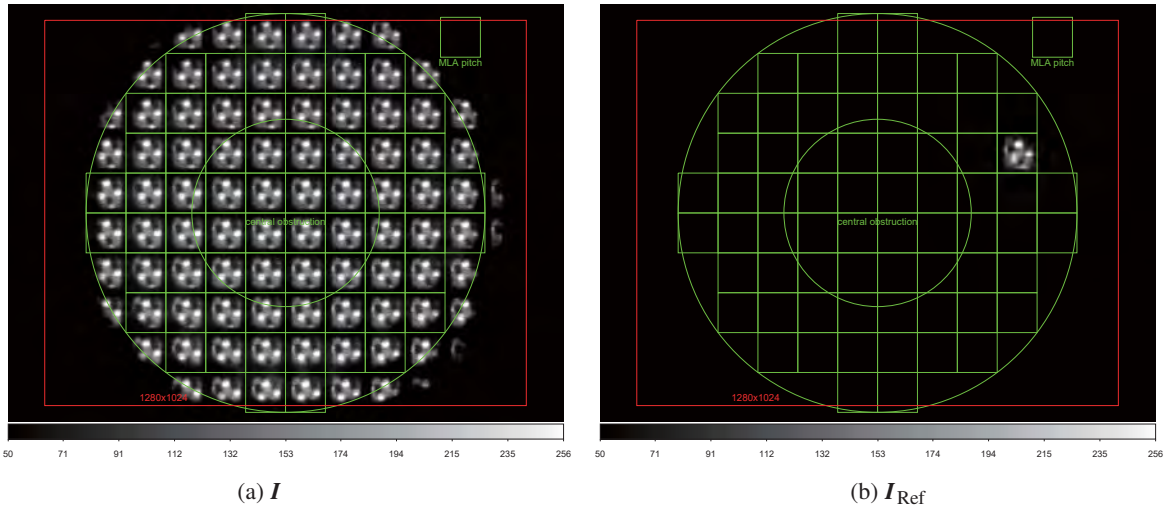
(a) $\boldsymbol{I}$ (b) $\boldsymbol{I}_{\text{Ref}}$

Fig. 10: Example of Hartmanngram – (a): all sub-images $\boldsymbol{I}$, (b): template sub-image $\boldsymbol{I}_{\text{Ref}}$.

shown in Fig. 11(a) and Fig. 11(b), respectively. Before calculating cross-correlation, the origin of the reference cell as shown in Fig. 10(b) must be shifted to the center in the Fourier domain.

$$\mathcal{I}_{\text{Ref}}(u,v)e^{-2\pi i[(p-0.5)Pu+(q-0.5)Pv]} \tag{10}$$

As a result, the cross-correlation function of Fig. 9(b) are arranged on the array as if it were a Hartmanngram of point light source. In this paper, we call this diagram of Fig. 11 as the cross-correlation Hartmanngram (CC-Hartmanngram) because it is similar to that of a point light source.
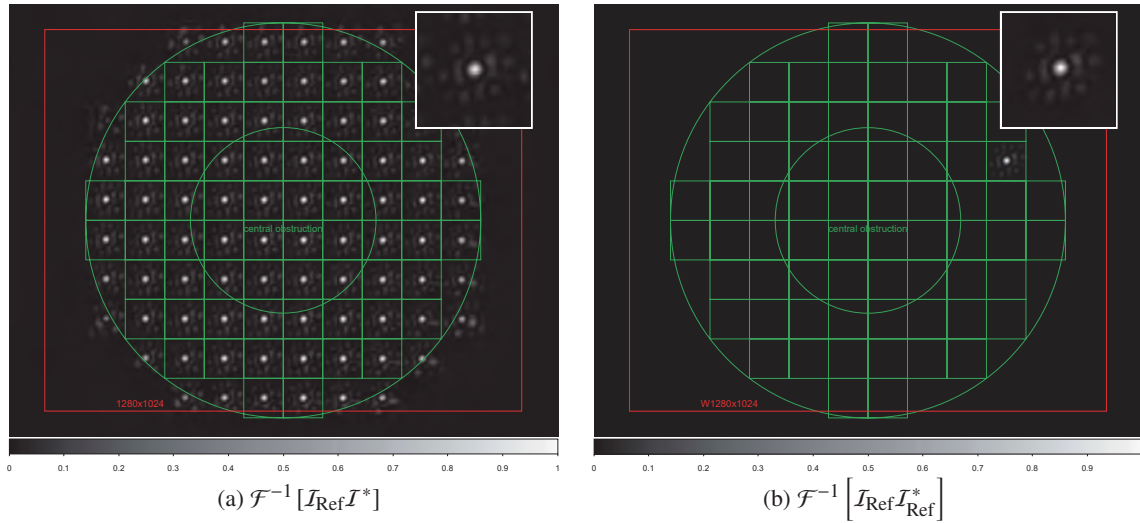

(a) $\mathcal{F}^{-1}\left[\mathcal{I}_{\text{Ref}}\mathcal{I}^*\right]$ (b) $\mathcal{F}^{-1}\left[\mathcal{I}_{\text{Ref}}\mathcal{I}_{\text{Ref}}^*\right]$

Fig. 11: Example of correlation function – (a): cross-correlation between $\boldsymbol{I}$ and $\boldsymbol{I}_{\text{Ref}}$, (b): auto-correlation of $\boldsymbol{I}_{\text{Ref}}$

4.2 Accuracy of wavefront sensing with extended scene

As described in Section 2.2, the accuracy of the wavefront measurement depends on an algorithm to obtain the relative displacement of the sub-image on the area sensor. Therefore, the object slides shown in Fig. 5 are shifted with given displacements vertically or horizontally in order to confirm the accuracy of relative displacement.

Fig. 12(a) and Fig. 12(b) show an zoomed view and a cross-sectional view of CC-Hartmanngram obtained from before and after movements, respectively. It can be seen that the correlation peak is slightly shifted to the left since the green

crosshair as shown in Fig. 12 is placed in the same position. The profile of the main peak is symmetric and also larger than that of the sub-peaks roughly by an order of magnitude. The resulting CC-Hartmanngram is similar to original Hartmanngram obtained from a point light source except that the correlation sub-peaks are aligned around the main peak.
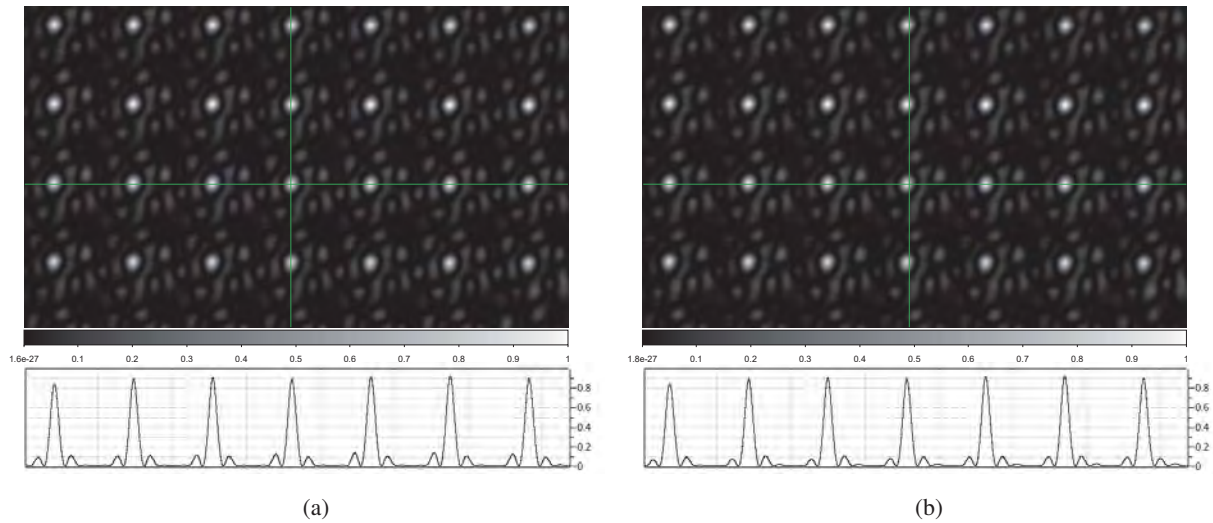

Fig. 12: Cross sectional view of CC-Hartmanngram E_{CC}.

In order to obtain the wavefront inclination θ, we next calculate the relative displacement δ from the CC-Hartmanngram. Fig. 13 shows the calculation flow of wavefront errors. In the case of WFS using a point light source, the displacement has been obtained by centroiding calculation (Fig. 13c) because the profile of spot sub-image (Fig. 13b) is symmetric. On the other hand, in the case of the extended light source, the relative displacement may be determined from the peak position of the cross-correlation function (Fig. 13h). However, CC-Hartmanngram (Fig. 13f) is similar to the Hartmanngram of point light source (Fig. 13b) as described before.

Because these correlation sub-peaks are so weak compared to the main peak, the contamination from sub-peaks can be negligible by setting the threshold level. Therefore, it was supposed that the relative displacement can be obtained from both the centroid (Fig. 13c) and the position of the correlation peak (Fig. 13h).
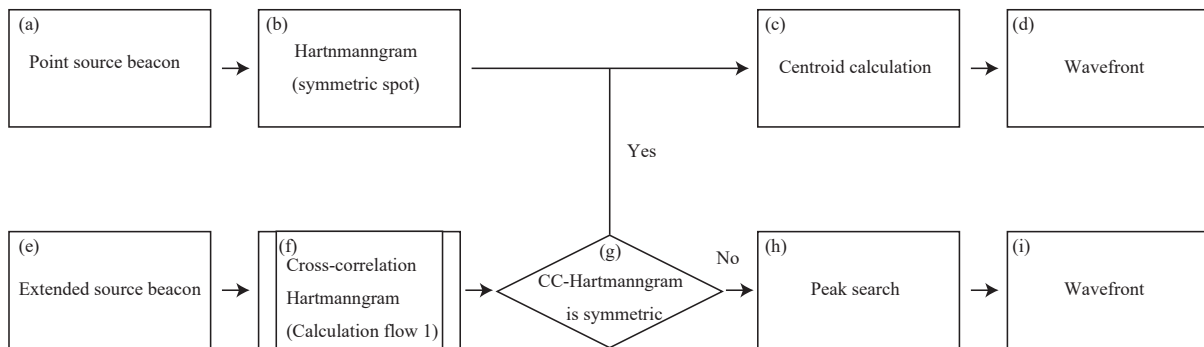

Fig. 13: Calculation flow 2

Fig. 14 shows the relationship between estimated displacement and given displacement of object slide. The movement of the object slide is plotted on the horizontal axis, and the displacement estimated by the centroiding calculation (Fig. 14a) or by searching the peak position (Fig. 14b) is plotted on the vertical axis. The open squares show the measurement positions and the solid line shows the best-fit value with the linear function. The lower panel of Fig. 14 shows the residuals from the best-fit model, and the broken line indicates the range of $\pm 1/20$ pixel and $\pm 1/50$ pixel. From

Fig. 14, the root mean square (RMS) error obtained by centroid position and peak position is (a) 0.01786 [pixel r.m.s] $\lesssim$ 1/55 [pixel r.m.s] and (b) 0.01435 [pixel r.m.s] $\lesssim$ 1/69 [pixel r.m.s], respectively.

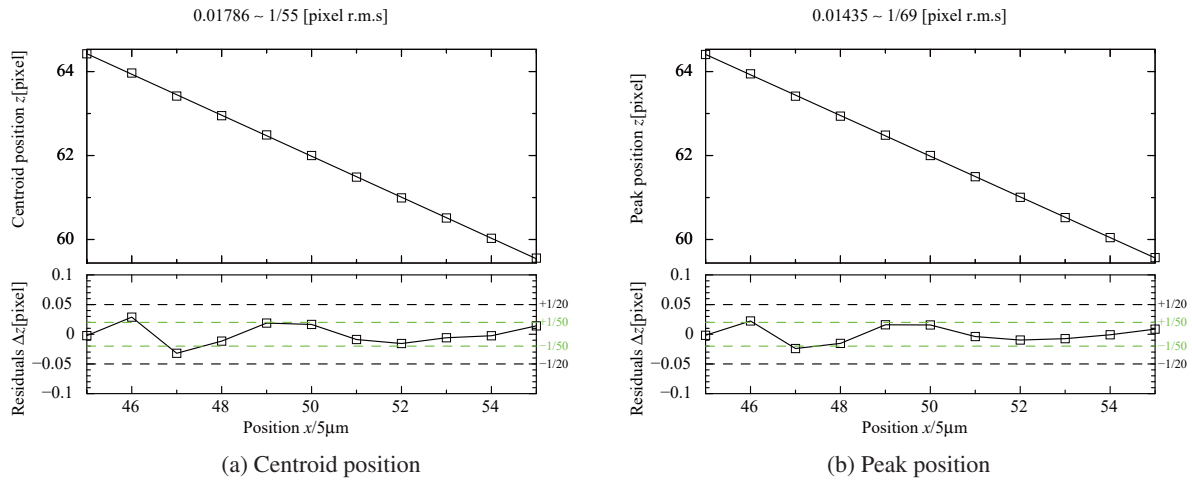(a) Centroid position   (b) Peak position

Fig. 14: Estimated sub-image positions and residuals.

Although details are omitted here, another study shows that the accuracy of $< 1/50$ [pixel r.m.s] is required to achieve the repeatability of $\leq 0.05\ \lambda$. In this case, it is considered that the first goal was achieved because the RMS error of 1/69 [pixel r.m.s] is satisfied with this criterion.

5.   CONCLUSION AND OUTLOOK

In order to measure the aberration of the space telescope during in-flight operation, we designed a prototype on-board WFS that refers to an extended source. Since the sub-images created on the area sensor by the extended source are asymmetric, the location of sub-image related to the incoming wavefront tilt cannot be determined by the centroid calculation. Therefore, we discussed here the correlation-based wavefront sensing algorithm and the preliminary results of the prototype SH-WFS for on-board satellite.

The accuracy of the wavefront measurement depends on an algorithm to obtain the relative displacement of the sub-image on the area sensor. In order to compensate up to the fifth order of Zernike polynomial with an accuracy of $5/100\ \lambda$, the accuracy of 1/50 pixel is required to measure the sub-pixel displacement of the sub-image. We thus evaluated the accuracy of the sub-pixel shift for prototype SH-WFS in the laboratory. As a result, it is confirmed that the RMS error evaluated from the cross-correlation of sub-image satisfy less than 1/69 pixel. It corresponds to measure the fifth-order aberration of the space telescope with an accuracy $4/100\ \lambda$.

As described in Section 4, note that the accuracy verified with experimental optics is not the wavefront aberration of the telescope optics itself, but the sub-pixel displacement of Hartmanngram. In order to confirm the accuracy of wavefront error, we have been modifying the control software designed for a conventional WFS to calculate the sub-image displacement by the cross-correlation algorithm. After software implementation is completed, we consider that realistic verification of aberration measurement can be performed by appending the wavefront errors due to thermal deformation and the misalignment of optical systems.

On the other hand, we also design the onboard SH-WFS to place in the optical payload of a satellite. Fig. 16 shows the onboard wavefront sensor in which the optical system is covered by a transparent housing structure for demonstration. In this prototype model, it is designed to verify both the function of wavefront sensing and accuracy of aberration measurement. In this paper, the main purpose is to verify the optical design and measurement accuracy of the wavefront. Therefore, we have considered that the first goal of the experiments was achieved because the RMS error was satisfied with this criterion. Furthermore, in order to mount on the space-based telescope, we should also consider that many problems such as operation in a thermal vacuum environment test, vibration test, and radiation resistance must be solved.
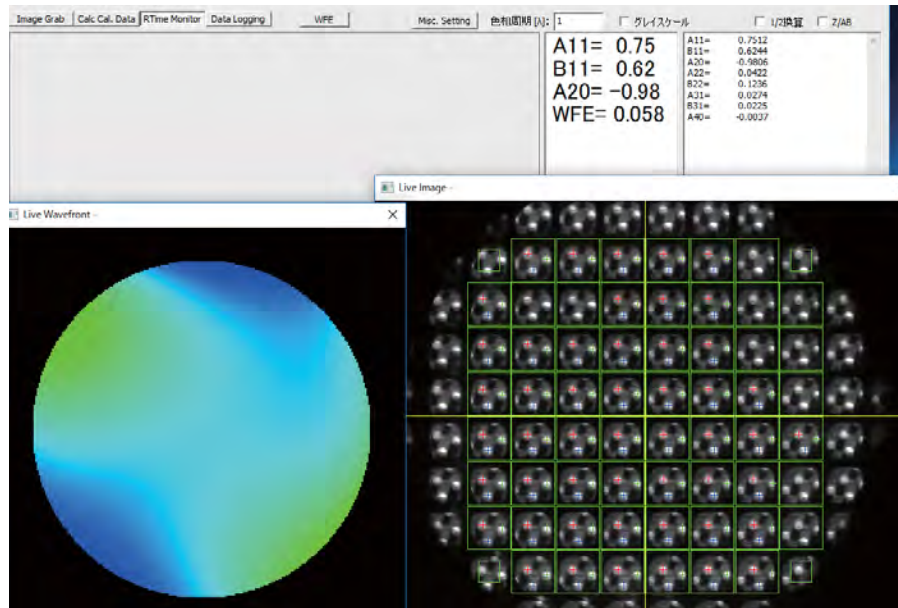
Fig. 15: Control software of extended scene SH-WFS.

Fig. 16: Prototype model of extended scene SH-WFS for onboard satellite.

6. REFERENCES

[1] A. Montmerle Bonnefois, T. Fusco, S. Meimon, V. Michau, L. Mugnier, J.-F. Sauvage, C. Engel, C. Escolle, M. Ferrari, E. Hugot, A. Liotard, M. Bernot, M. Carlavan, F. Falzon, T. Bret-Dibat, and D. Laubier., Comparative theoretical and experimental study of a shack-hartmann and a phase diversity sensor, for high-precision wavefront sensing dedicated to space active optics. *Proc SPIE*, 105634B, 2017.

[2] N. Miura, A. Oh-ishi, S. Kuwamura, N. Baba, Y. Hanaoka, Y. Ueno, S. Nakatani, and K. Ichimoto., Status of hida solar adaptive optics system and experiment of tomographic wavefront sensing., *Proc SPIE*, 99092N, 2016.

[3] E. Sidick., Adaptive periodic-correlation algorithm for extended scene shack-hartmann wavefront sensing, Imaging and Applied Optics, *OSA Technical Digest*, CPDP1, 2011.

[4] R. Tyson., *Principles of adaptive optics, Fourth edition*. CRC press, 2015.

[5] S. Thomas, T. Fusco, A. Tokovinin, M. Nicolle, V. Michau, and G. Rousset., Comparison of centroid computation algorithms in a Shack-Hartmann sensor., *MNRAS*, Vol 371, 323–336, 2006.

[6] Y. Asari, Y. Katsuki, and T. Shimizu., Telescope driving control technology to realize a high celestial body tracking accuracy (in japanese)., *Mitsubishi Denki Giho*, Vol 73, 19–22, 1999.

[7] T. Endo, Y. Miwa, J. Suzuki, T. Ando, T. Takanezawa, and Y. Ezaki., Improving Techniques for Shack-Hartmann Wavefront Sensing: Dynamic-Range and Frame Rate., *The Advanced Maui Optical and Space Surveillance Technologies Conference*, 964–973, 2018.

[8] J. Suzuki, T. Ando, H. Suzuki, Y. Hirano, S. Wadaka, T. Matsushita, and I. Mikami., Highly precise alignment method for a space telescope using shack-hartmann sensor (in japanese)., *KOGAKU*, Vol 35, 534–541, 2006.

[9] N. Takato, T. Usuda, and W. Tanaka., Performance of active mirror support of Subaru Telescope., *Proc SPIE*, Vol 4837, 675–680, 2003.